




Article

Revisiting the Performance of the Kernel-Driven BRDF Model Using Filtered High-Quality POLDER Observations

Hanliang Li ¹, Kai Yan ^{1,*}, Si Gao ¹, Wanjuan Song ² and Xihan Mu ³

¹ School of Land Science and Techniques, China University of Geosciences, Beijing 100083, China; lihanliang1998@cugb.edu.cn (H.L.); gaosi_2021@email.cugb.edu.cn (S.G.)

² State Key Laboratory of Remote Sensing Science, Aerospace Information Research Institute, Chinese Academy of Sciences, Beijing 100101, China; songwj@aircas.ac.cn

³ State Key Laboratory of Remote Sensing Science, Faculty of Geographical Science, Beijing Normal University, Beijing 100875, China; muxihan@bnu.edu.cn

* Correspondence: kaiyan@cugb.edu.cn

Abstract: The Bidirectional Reflectance Distribution Function (BRDF) is usually used to describe the reflectance anisotropy of a non-Lambertian surface and estimate surface parameters. Among the BRDF models, the kernel-driven models have been extensively used due to their simple form and powerful fitting ability, and their reliability has been validated in some studies. However, existing validation efforts used in situ measurements or limited satellite data, which may be subject to inadequate observational conditions or quality uncertainties. A recently released high-quality BRDF database from Polarization and Directionality of the Earth's Reflectances (POLDER) provides an opportunity to revisit the performance of the kernel-driven models. Therefore, in order to evaluate the fitting ability of the kernel-driven models under different observational conditions and explore their application direction in the future, we use the filtered high-quality BRDF database to evaluate the fitting ability of the kernel-driven model represented by the RossThick-LiSparseR (RTLSR) kernels in this paper. The results show that the RTLSR model performs well, which shows small fitting residuals under most observational conditions. However, the applicability of the RTLSR model performed differently across land cover types; the RTLSR model exhibited larger fitting residuals, especially over non-vegetated surfaces. Under different sun-sensor geometries, the fitting residuals show a strong positive correlation with the Solar Zenith Angle. The above two factors cause the RTLSR model to exhibit a poorer fitting ability at high latitudes. As an exploration, we designed a model combination strategy that combines the advantages of different models and achieved a better performance at high latitudes. We believe that this study provides a better understanding of the RTLSR model.

Keywords: applicability comparison; BRDF; kernel-driven model; POLDER



Citation: Li, H.; Yan, K.; Gao, S.; Song, W.; Mu, X. Revisiting the Performance of the Kernel-Driven BRDF Model Using Filtered High-Quality POLDER Observations. *Forests* **2022**, *13*, 435. <https://doi.org/10.3390/f13030435>

Academic Editor: Gang Chen

Received: 27 January 2022

Accepted: 8 March 2022

Published: 10 March 2022

Publisher's Note: MDPI stays neutral with regard to jurisdictional claims in published maps and institutional affiliations.



Copyright: © 2022 by the authors. Licensee MDPI, Basel, Switzerland. This article is an open access article distributed under the terms and conditions of the Creative Commons Attribution (CC BY) license (<https://creativecommons.org/licenses/by/4.0/>).

1. Introduction

The Bidirectional Reflectance Distribution Function (BRDF) is defined as the ratio of the radiance in the direction of the exit beam to the irradiance caused by the entrance beam [1]. In remote sensing, BRDF commonly represents the distribution of bidirectional reflectance to quantify surface reflectance anisotropy [2]. An accurate estimate of land surface BRDF serves to correct the bidirectional effects in vegetation indices and reflectance and to estimate land surface physical, biological parameters, and vegetation structural parameters, such as albedo and leaf area index (LAI) from reflectance measurements [3–7]. Therefore, accurate modeling of the global land surface BRDF is important for global ecosystem monitoring and radiation balance researches.

Several empirical, semi-empirical, and physical methods have been developed for BRDF modeling. Among them, the semi-empirical linear kernel-driven models introduced by Roujean et al. [8] have been widely used. Wanner et al. [9] and Lucht et al. [6] subsequently improved the kernel-driven model to make it easier to understand and apply as the Algorithm for Model Bidirectional Reflectance Anisotropies of the Land Surface (AMBRALS) [10]. The kernel-driven models were adopted as the operational algorithms for generating land surface albedo products by many spaceborne sensors, including the Moderate Resolution Imaging Spectroradiometer (MODIS) and Polarization and Directionality of the Earth's Reflectances (POLDER) [6,11–16]. Scholars developed many kernels to describe the radiative transfer process of different scenes, such as the well-known Ross kernels and Li kernels [6,8,17]. Li et al. [17,18] also developed a kernel called the LiTransit kernel to describe the geometric–optical relationships of discrete canopies under large zenith angles better. Meanwhile, Maignan et al. [19] and Jiao et al. [20] further modified the hotspot effect of the kernel-driven model. In addition, there were some new models based on the form of kernel-driven models to describe the radiative transfer process of a certain scenario better [21,22], which can also be regarded as an extended form of kernel-driven models.

The reliability of the kernel-driven models was validated using multiangle datasets and field measurements [23–25]. However, existing validation efforts used in situ measurements or limited satellite data, which may be subject to inadequate observational conditions or quality uncertainties. This resulted in applicability differences of kernel-driven models under different observational conditions not being adequately compared. This requires high-quality, large-scale global observations from the same sensor to remove the interference from data uncertainty as much as possible. The publication of a high-quality POLDER BRDF database, which is recommended for assessing the typical variabilities of natural surface reflectances and evaluating models, provides an opportunity for a more comprehensive applicability comparison of the kernel-driven model to revisit its performance under different observational conditions [26]. This database provides a set of filtered high-quality reflectance observations with various observation geometries from the POLDER-3 sensor. The observations in this database are representative and of a high quality, and have been used for model validation and bidirectional surface reflectance evaluations [21,27,28]. At the same time, most of the current large-scale researches or product production used only a single kernel-driven model [29,30]. However, as noted above, while many types of kernel-driven models have been developed, to date, to adapt to different observational conditions, studies on the joint application of kernel-driven models are still insufficient and require further exploration. Therefore, the primary objective of this paper is to revisit the fitting ability of the kernel-driven models under different observational conditions using high-quality global observations, and thereby explore its application and future directions.

In this study, we compare the applicability of the kernel-driven model represented by RossThick-LiSparseReciprocal (RTLSR) kernels under different observational conditions using the POLDER BRDF database. As an exploration, a Simple Joint Retrieval Strategy (SJRS), based on the applicability comparison results, is proposed to compensate for the shortcomings of using the RTLSR model alone, which could serve as a guide for continuous improvement of the RTLSR model. This paper is organized as follows. Section 2 introduces the necessary information and mathematical formulas of the kernel-driven models, database, and comparative analysis method, as well as describes the general design idea of the SJRS in detail. Section 3 presents the results of the model applicability comparison. In Section 4, we thoroughly discuss the results of the experiments, the potential of the joint application of multiple models, and future perspectives of kernel-driven models. Finally, the limitations of our experiment are also summarized.

2. Materials and Methods

2.1. POLDER BRDF Database

In this study, we used a high-quality BRDF database published by Breon et al. [26], which is recommended by the authors to be applied in assessing the typical variabilities of

natural surface reflectances or evaluating the new BRDF models (<https://doi.pangaea.de/10.1594/PANGAEA.864090> (accessed on 27 January 2022)). This database provides a set of high-quality reflectance observations from the POLDER-3 sensor collected from January 2008 to December 2008. It only includes observations from 2008, as this year was the best in terms of data acquisition continuity. Moreover, these observations are available without significant cloud or aerosol contamination and were acquired with various observation geometries. The targets are classified into 16 classes of IGBP (International Geosphere-Biosphere Programme) land cover types (without water), the selection of which requires spatial representativeness within the class [14]. The POLDER-3 observes the surface target from up to 16 directions (14 on average) per overflight with a maximum View Zenith Angle (VZA) close to 70° [26]. These allow us to easily compare the fitting ability of the RTLSR model over different land cover types and observation geometries.

The BRDF database contains six bands of reflectance data, and only the red and Near-Infrared (NIR) bands (centered at 670 nm and 865 nm, respectively) were used in this study. It also provides a metric called Aero, which is a non-quantitative indication of the aerosol load retrieved from POLDER measurements. Aero = 0 means minimal aerosol load, whereas Aero = 15 represents a high aerosol load. Only observations with Aero ≤ 5 are used in our study. Figure 1 shows the global distribution of POLDER BRDF database sites.

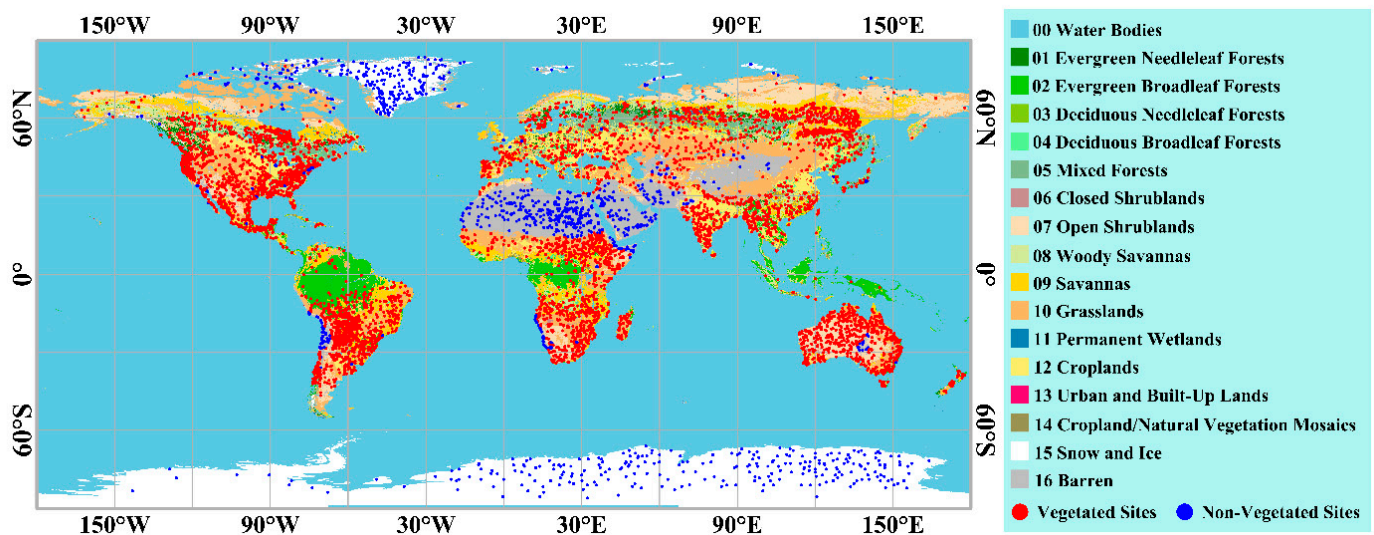


Figure 1. Global distribution of the selected POLDER BRDF database sites over the MODIS IGBP land cover map. The red and blue points represent the data in vegetated and non-vegetated lands, respectively.

2.2. Linear Kernel-Driven Models and Retrieval Method

In optics, BRDF is defined as the ratio of the radiance in the direction of the exit beam to the irradiance caused by the entrance beam [1]. However, it cannot be strictly measurable under natural conditions. It essentially describes the anisotropy of the irradiated object. In remote sensing, since pixels are usually non-uniform surfaces with a certain area, the BRDF cannot be defined effectively, while the definition of parameters, such as reflectance, still holds. Therefore, the measured reflectance data are often referred to as BRDF [31,32]. BRDF is usually used to represent the bidirectional reflectance distribution to quantitatively describe the anisotropy of the land surface [22,33]. The linear kernel-driven model, originally proposed by Roujean et al. [8], is usually used to retrieve bidirectional reflectance. It can be formalized as the empirically weighted sum of several scattering components [34]. The equation can be expressed as:

$$R(\theta_s, \theta_v, \varphi, \lambda) = f_{iso}(\lambda) + f_{vol}(\lambda)K_{vol}(\theta_s, \theta_v, \varphi) + f_{geo}(\lambda)K_{geo}(\theta_s, \theta_v, \varphi) \quad (1)$$

where $R(\theta_s, \theta_v, \varphi, \lambda)$ is the reflectance in waveband λ , which is a function of the Solar Zenith Angle (SZA) θ_s , VZA θ_v , and Relative Azimuth Angle (RAA) φ . $f_{iso}(\lambda)$, $f_{vol}(\lambda)$, and $f_{geo}(\lambda)$ are the weight components of the isotropic scattering kernel (considered as 1), volume-scattering kernel $K_{vol}(\theta_s, \theta_v, \varphi)$, and geometric-optical kernel $K_{geo}(\theta_s, \theta_v, \varphi)$.

Given reflectance observations $\rho(\theta_s, \theta_v, \varphi, \lambda)$, the minimization $\frac{\partial e^2}{\partial f_k} = 0$ of a least-squares error function:

$$e^2(\lambda) = \frac{1}{d} \sum_l \frac{(\rho_l(\theta_s, \theta_v, \varphi, \lambda) - R_l(\theta_s, \theta_v, \varphi, \lambda))^2}{w_l(\lambda)} \tag{2}$$

leads to analytical solutions for the weight components f_k of the kernels:

$$f_k(\lambda) = \sum_i \left\{ \sum_j \frac{\rho_j(\theta_s, \theta_v, \varphi, \lambda) K_j(\theta_s, \theta_v, \varphi)}{w_j(\lambda)} \times \left(\sum_l \frac{K_l(\theta_s, \theta_v, \varphi) K_k(\theta_s, \theta_v, \varphi)}{w_l(\lambda)} \right)^{-1} \right\} \tag{3}$$

where $w_l(\lambda)$ is the weight given to each observation. In this study, all eligible observations were given the same weight [6]. Additionally, d are the degrees of freedom (number of observations minus number of parameters f_k).

Some extended forms of the kernel-driven model typically introduce more input parameters or kernels to improve fitting ability. Therefore, Equation (1) may not be a general form of the kernel-driven models. In this paper, the kernel-driven models can be considered as a general term for models that work in the same way (kernel drive).

2.2.1. RTLSR Model

The RTLSR model is widely used for its excellent fitting ability among many kernel-driven models, which consists of the volume-scattering kernel RossThick and the geometric-optical kernel LiSparseReciprocal. The RossThick kernel was derived by Roujean et al. [8] based on the radiative transfer theory of Ross [35], which is used to calculate the bidirectional reflectance above a horizontally homogeneous plant canopy with large values of the LAI (the formula for the RossThick kernel is given in detail in Appendix A). The LiSparseReciprocal kernel is a reciprocal form of the geometric-optical kernel LiSparse [6,17,36]. The LiSparse kernel is the approximation of a geometric-optical mutual shadowing model by Li and Strahler [37] derived by Wanner et al. [9]. It is modeled as:

$$K_{LiSparse} = O(\theta_s', \theta_v', \varphi) - \sec \theta_s' - \sec \theta_v' + \frac{1}{2}(1 + \cos \zeta') \sec \theta_v' \\ = P(\theta_s', \theta_v', \varphi) \sec \theta_v' - B(\theta_s', \theta_v', \varphi) \tag{4}$$

where $B(\theta_s', \theta_v', \varphi) = \sec \theta_s' + \sec \theta_v' - O(\theta_s', \theta_v', \varphi)$, $P(\theta_s', \theta_v', \varphi) = \frac{1}{2}(1 + \cos \zeta')$ and

$$O = \frac{1}{\pi} (t - \sin t \cos t) (\sec \theta_s' + \sec \theta_v') \tag{5}$$

$$\cos t = \frac{h}{b} \frac{\sqrt{D^2 + (\tan \theta_s' \tan \theta_v' \sin \varphi)^2}}{\sec \theta_s' + \sec \theta_v'} \tag{6}$$

$$D = \sqrt{\tan^2 \theta_s' + \tan^2 \theta_v' - 2 \tan \theta_s' \tan \theta_v' \cos \varphi} \tag{7}$$

$$\cos \zeta' = \cos \theta_s' \cos \theta_v' + \sin \theta_s' \sin \theta_v' \cos \varphi \tag{8}$$

$$\theta_{s,v}' = \tan^{-1} \left(\frac{b}{r} \tan \theta_{s,v} \right) \tag{9}$$

$$\varphi = \text{abs}(\varphi_s - \varphi_v), 0 \leq \varphi < \pi \tag{10}$$

where φ_s and φ_v are the solar and view azimuth angles. The LiSparse kernel was designed for sparsely located clumps and associated shadows. The approximation made for LiSparse

is $e^{-x} = 1 - x$, where x is the area proportion of this clump plus shadow, roughly proportional to $\sec \theta_v$. Therefore, LiSparse kernel has poor ability for extrapolation at large VZAs, especially when SZA is large, where negative reflectance may appear even the kernel fits the sampled observations very well. To alleviate this problem, the LiSparseReciprocal kernel was proposed based on the reciprocity principle [38]. The kernel is modeled as:

$$K_{\text{LiSparseR}} = P(\theta_s', \theta_v', \varphi) \sec \theta_s' \sec \theta_v' - B(\theta_s', \theta_v', \varphi) \quad (11)$$

In the above equations, the parameters $\frac{b}{r}$ and $\frac{h}{b}$ are used to describe the relative crown shape and relative crown height, respectively. The LiSparseReciprocal kernel set to $\frac{b}{r} = 1$ and $\frac{h}{b} = 2$ is adopted by the MODIS BRDF/albedo algorithm, which is also used in this study. More details on the derivation of this kernel can be found in [9].

2.2.2. RTLTL Model

The Helmholtz principle of reciprocity has been proved that it suffers scale effect over the heterogeneous land surface and thus does not generally apply to the scale of a remote-sensing pixel [39]. To address this issue, Li et al. [17] improved a new kernel with better extrapolation capabilities, LiTransit, which is proposed to replace the LiSparseReciprocal kernel in the next version of AMBRALS. The RTLTL model was generated by combining the volume-scattering kernel RossThick and the geometric-optical kernel LiTransit. The LiTransit kernel can be expressed as:

$$K_{\text{LiTransit}} = \begin{cases} K_{\text{LiSparse}}, & B(\theta_s', \theta_v', \varphi) \leq 2 \\ \frac{2 \cdot K_{\text{LiSparse}}}{B(\theta_s', \theta_v', \varphi)}, & B(\theta_s', \theta_v', \varphi) > 2 \end{cases} \quad (12)$$

In this paper, the RTLTL model is tried to process the data with large SZA.

2.2.3. RTLSRS Model

The RTLSRS (RossThick-LiSparseR-Snow) model developed by Jiao et al. [21] was designed to characterize the scattering properties of the snow surface better. The snow kernel in the model can be seen as a correction kernel based on the Asymptotic Radiative Transfer (ART) model, which assumes that snow can be modeled as a semi-infinite, plane-parallel, weakly absorbing light scattering layer. The snow kernel adopts a correction term with a free parameter α to correct the analytic form of the ART model. The snow kernel and RTLSRS model can be written as follows:

$$K_{\text{snow}} = R_0(\theta_s, \theta_v, \varphi)(1 - \alpha \cdot \cos \xi \cdot e^{-\cos \xi}) + 0.04076\alpha - 1.1081 \quad (13)$$

$$R(\theta_s, \theta_v, \varphi, \lambda) = f_{\text{iso}}(\lambda) + f_{\text{vol}}(\lambda)K_{\text{vol}}(\theta_s, \theta_v, \varphi) + f_{\text{geo}}(\lambda)K_{\text{geo}}(\theta_s, \theta_v, \varphi) + f_{\text{snow}}(\lambda)K_{\text{snow}}(\theta_s, \theta_v, \varphi) \quad (14)$$

where R_0 refers to the surface reflectance of a semi-infinite, non-absorbing media layer at zero absorption. In this paper, the α was set to 0.3 as recommended [21]. The RTLSRS model with the additional snow kernel can be seen as an extended form of the kernel-driven models.

2.3. Comparative Analysis

The kernel-driven models can fit the kernel coefficients by taking the reflectance and sun-sensor geometries data from the POLDER BRDF database as the input data [6]. This database contains data at different sites for different months and IGBP (detailed information on how they are organized can be found in [26]). The coefficients of the kernel-driven model were calculated using one-month valid data for each site. We then used these coefficients to retrieve the corresponding reflectance. By comparing the retrieved reflectance with observational reflectance, the applicability of the RTLTL model in different scenarios can be evaluated. The NDVI (Normalized Difference Vegetation Index) was used to characterize the vegetation densities. The fitting ability of the RTLTL model was

comprehensively compared under different IGBP and NDVI, sun-sensor geometries, and spatial and temporal conditions. For statistical data analysis, we restricted only 20 or more eligible sites to participate, and eligible sites must have at least 16 observations with a low aerosol load ($Areo \leq 5$).

We quantified the model fitting residuals using the Root-Mean-Square-Error (RMSE), and defined an Optimization Ratio (OR) for comparing the performance of other models with the RTLSR model. The corresponding formulas are as follows:

$$RMSE = \sqrt{\frac{1}{n-1} \sum_{i=1}^n (y_i - x_i)^2} \quad (15)$$

$$OR = \frac{RMSE_{RTLSR} - RMSE_{Other}}{RMSE_{RTLSR}} \times 100\%$$

where n is the number of reflectances, and x and y are the observed and retrieved reflectances, respectively. $RMSE_{RTLSR}$ and $RMSE_{Other}$ are the RMSE of RTLSR and other models, respectively.

2.4. Simple Joint Retrieval Strategy

In the results of the adaptability comparison of the RTLSR model to different observational conditions (shown in Section 3.1), the model shows a poor fitting ability to non-vegetated surfaces and large SZA conditions. This makes the model exhibit larger fitting residuals at high latitudes. As an exploration, we designed the SJRS and its workflow is shown in Figure 2.

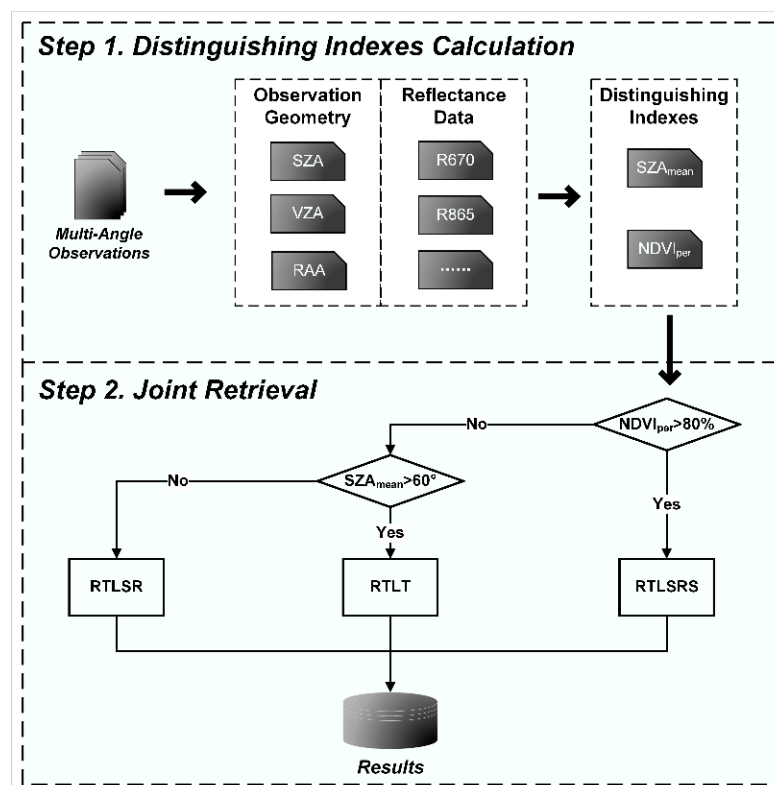


Figure 2. Workflow of the Simple Joint Retrieval Strategy (SJRS). SZA_{mean} is the mean Solar Zenith Angle (SZA) of the observations at the site. $NDVI_{per}$ is the percentage of the observations with Normalized Difference Vegetation Index (NDVI) < 0 at the site. RAA is Relative Azimuth Angle. R670 and R865 mean the reflectance in red (670 nm) and NIR (865 nm) bands. RTLSR, RTLTL, and RTLSRS are the models mentioned in Section 2.2.

First, we extracted the reflectance and observation geometry information in red and NIR bands from the quality-controlled POLDER sites. Then, the mean SZA (SZA_{mean}) and the percentage of NDVI less than 0 at each site ($NDVI_{\text{per}}$) were calculated. We used $NDVI_{\text{per}}$ to determine whether the site is widely covered by snow or ice. If $NDVI_{\text{per}}$ is greater than 80%, the SJRS would use the RTLSRS model to process it. Otherwise, we would further determine whether SZA_{mean} is greater than 60° , if yes, the site would be retrieved using RTLT. If SZA_{mean} is less than 60° , the RTLSR model would be used. Finally, the results of each model are integrated into the retrieval results for the global land surface sites. It is worth noting that the thresholds SZA_{mean} and $NDVI_{\text{per}}$ are adjustable parameters. In this paper, they were set to 60° and 80% empirically for the initial exploration of the joint application of the multiple models.

3. Results

3.1. Applicability Comparison of the RTLSR Model

In this section, the POLDER database was used to revisit the fitting ability of the RTLSR model under different observational conditions. The relevant results are given in Figures 3–5. The performance of the RTLSR model over different land covers is given in Figure 3. Overall, the mean fitting residuals of the RTLSR model for all scenarios are 0.0139 and 0.0159 in the red and NIR bands, respectively, indicating a good fitting ability of RTLSR. However, it can be noted that the RTLSR model shows larger fitting residuals in both the red (Figure 3(a-1)) and NIR (Figure 3(a-2)) bands over snow and ice, urban and built-up lands, and evergreen needleleaf forests. Especially for urban and built-up lands, the RMSE is up to 0.1298 (red) 0.0995 (NIR). This is due to the fact that the RTLSR model does not fit well to land covers with large forward scattering. The fitting residuals of the RTLSR model are relatively small over other land covers. For all NDVI levels, the fitting residuals are small over open shrublands and woody savannas. At the same time, the fitting residuals decreased as NDVI increased, as in urban and built-up lands, deciduous broadleaf forests, and mixed forests in the red band. For a more intuitive representation, the fitting residuals of the RTLSR model in vegetated and non-vegetated lands, classified into three levels of vegetation density based on the NDVI values, can be seen in Figure 3(b-1,b-2). The RTLSR model shows lower fitting residuals over vegetated lands, and the fitting residuals decrease with increasing vegetation density. Over non-vegetated lands, the RMSE reaches 0.0424 when $NDVI < 0.3$ and decreases to 0.0090 when the $NDVI > 0.3$ in the red band. In the three NDVI levels of vegetated lands, the RMSE is 0.0126, 0.0085, and 0.0042, respectively. The phenomenon also exists for the NIR band: the RMSE is 0.0351 on the non-vegetated lands when $NDVI < 0.3$ and decreases to 0.0093 when $NDVI > 0.3$. For the three NDVI levels of vegetated lands, the RMSE is 0.0137, 0.0111, and 0.0102, respectively. In summary, the RTLSR model shows stronger adaptability to densely vegetated lands.

We also explored the influence of sun-sensor geometries on the fitting ability of the RTLSR model, as they are the input parameters of the kernel functions. The relationship between the sun-sensor geometries and the fitting residuals of the RTLSR model in the red (Figure 4a) and NIR (Figure 4b) bands were analyzed. In Figure 4(a-1,b-1), for a given RAA, the color of the dots changes from dark blue to red as the SZA increases from 0° to 75° , which means the values of the RMSE increase with SZA. Figure 4(a-2,b-2) show the change in fitting residuals when the VZA of the retrieved observations are different for a given RAA. The relationship between the fitting residuals and VZA is not clear. From the above statistics, it can be seen that the variations of the SZA greatly affect the fitting ability of the RTLSR model, and the fitting residuals of the RTLSR model increase when SZA becomes larger. Therefore, when SZA is large, the applicability of the RTLSR model needs to be further considered.

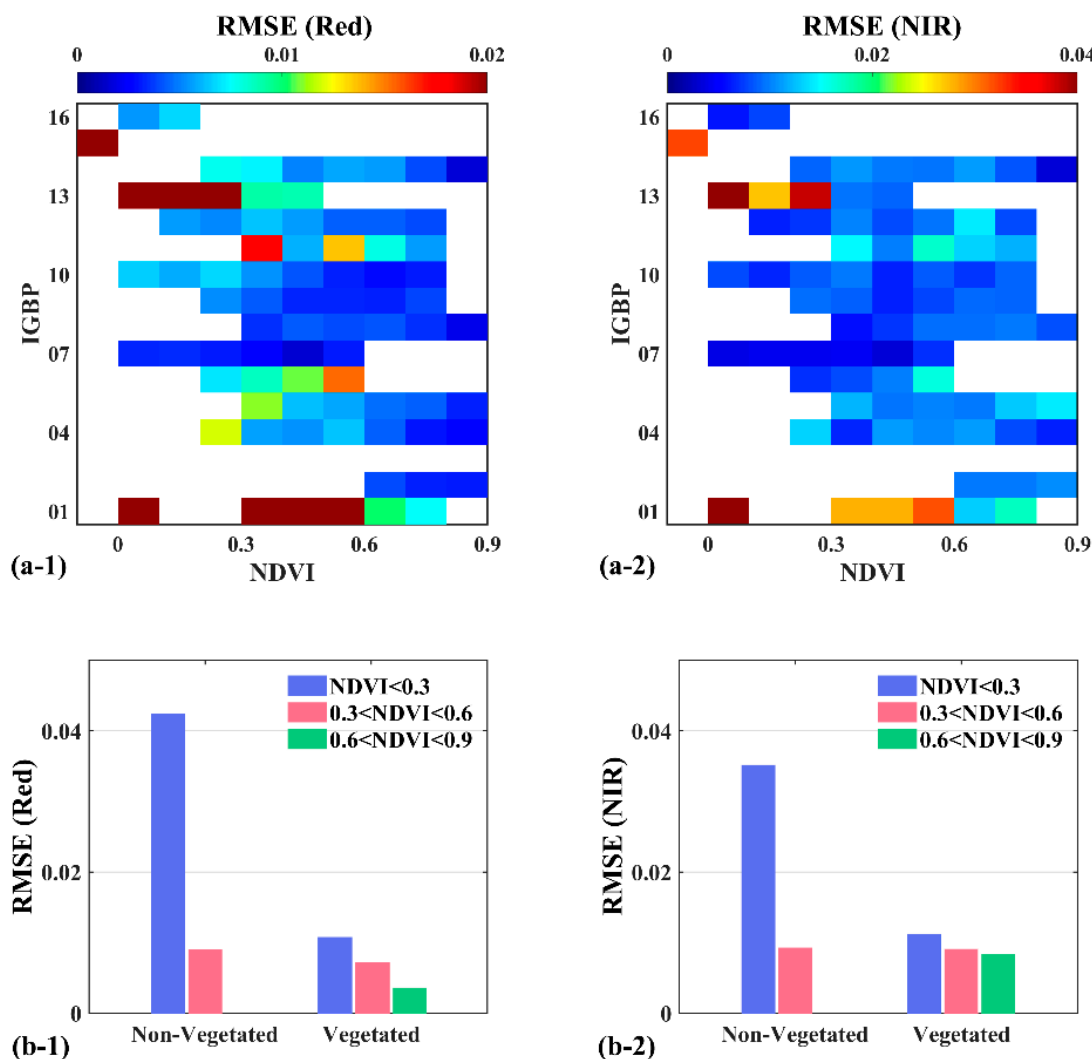


Figure 3. Fitting residuals of the RTLSR model for different land covers and NDVI levels in the red (1) and NIR (2) bands; (a-1,a-2) are values of the fitting residuals over different IGBP types, the colors correspond to RMSE values from low (blue) to high (red), and the blank areas mean no data. (b-1,b-2) show the fitting residuals of the RTLSR model on non-vegetated and vegetated lands. IGBP list: 01 Evergreen Needleleaf Forests; 02 Evergreen Broadleaf Forests; 03 Deciduous Needleleaf Forests; 04 Deciduous Broadleaf Forests; 05 Mixed Forests; 06 Closed Shrublands; 07 Open Shrublands; 08 Woody Savannas; 09 Savannas; 10 Grasslands; 11 Permanent Wetlands; 12 Croplands; 13 Urban and Built-Up Lands; 14 Cropland/Natural Vegetation Mosaics; 15 Snow and Ice; and 16 Barren.

Climate, land cover, vegetation density, and sun-sensor geometry are affected by latitude and time, which means that the RTLSR model should have different applicability at different latitudes and times. In the present study, we analyzed the spatial and temporal characteristics of the fitting residuals of the RTLSR model using observations at different latitudes and times (Figure 5). It can be found that the larger fitting residuals are at the four corners in the heat maps of the red and NIR bands. As the top line plot show, the mean fitting residuals of RTLSR reach 0.0444 and 0.0483 at high latitudes in the red and NIR bands, respectively. The reason should be that at high latitudes the land cover is mainly non-vegetated lands (wasteland or snow and ice) and vegetation is sparse, the SZA is also larger. The mean fitting residuals on different months are reflected in the right line plot in the red band (Figure 5a). The relationship between RMSE and time is weak. This suggests that the adaptability of the RTLSR model is not strongly correlated with time. Similar laws

are presented in the NIR band (Figure 5b). The results reflected in Figure 5 are consistent with the previous analysis.

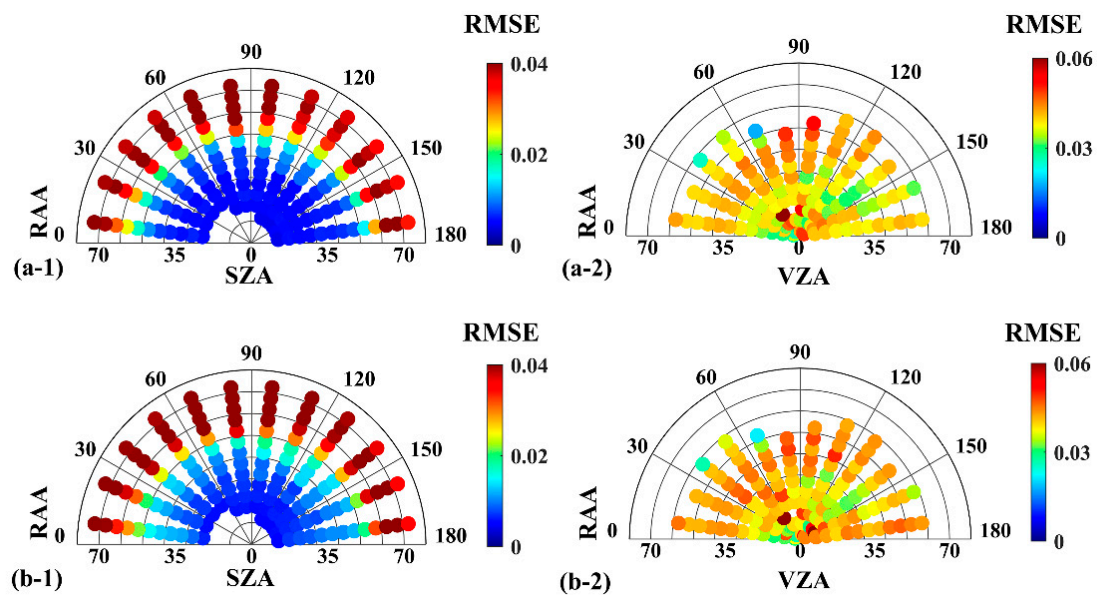


Figure 4. Fitting residuals of the RTLSR model in different sun-sensor geometries in the red (a) and NIR (b) bands. (a-1,b-1) are the fitting residuals when SZA is different for a given RAA. (a-2,b-2) are the fitting residuals when VZA is different for a given RAA. In the plots, the radii orient with the RAA and the concentric circles corresponding to the SZA (1) or VZA (2). The missing dots mean no data. The colors correspond to RMSE values from low (blue) to high (red).

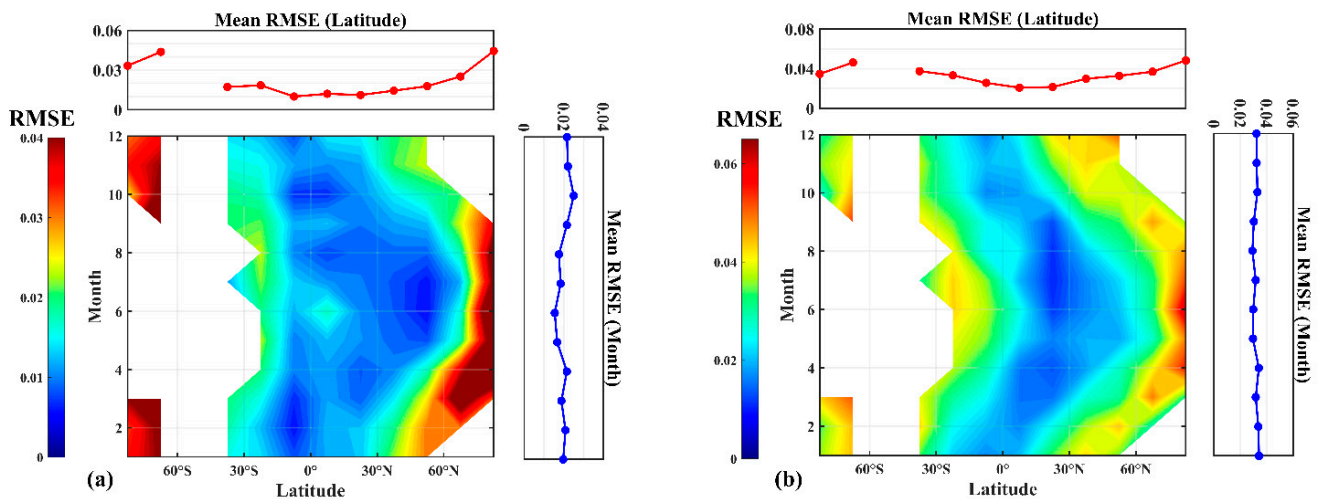


Figure 5. Comparison of the fitting residuals of the RTLSR model at different latitudes and months in the red (a) and NIR (b) bands. The colored bars represent RMSE values. The mean RMSE variation in different latitudes and months in the two bands are shown in the line plots above and to the right of the heatmaps, respectively.

3.2. Joint Application of Kernel-Driven Models

The RTLSR model performs well under most of the observational conditions. It still exhibits large errors at high latitudes due to changes in the land cover and observation geometry. In this section, whether the SJRS can compensate for the shortcomings of a single model is explored. The relevant results are presented in Figures 6–8. In Figure 6, the RTLSR and RTLT models are compared using quality-controlled observations with large SZA ($SZA > 60^\circ$). In the red band (Figure 6a), with the 30% RE (Relative Error) lines as the

reference, the predicted results of the RTLT model are more concentrated around the 1:1 line compared to those of the RTLSR model. This means that the predicted reflectance of the RTLSR model deviates more from the POLDER observed reflectance. The results statistics show that the mean RMSE of the RTLSR model in the red band is 0.0231, while the mean RMSE of the RTLT model is 0.0213. This finding is similar in the NIR band (Figure 6b): the mean RMSE of the RTLSR model is 0.0373, while the mean RMSE of the RTLT model is 0.0350. These suggest that the RTLT model does have more reliable extrapolation capability compared to the RTLSR model, and can retrieve these observed data with large SZA conditions more accurately.

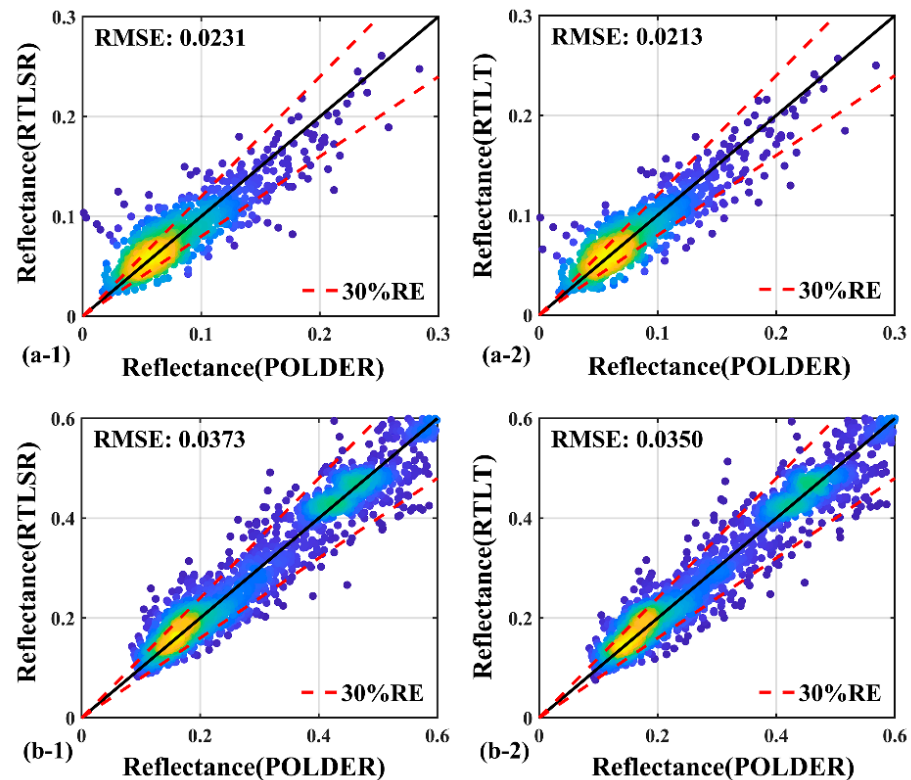


Figure 6. Comparison of the reflectance predicted by RTLSR and RTLT with POLDER observations using data with large SZA. The red dotted lines mean 30% RE. The colors correspond to point density from lowest (blue) to highest (yellow). The horizontal axes represent the reflectance from POLDER. The vertical axes represent the reflectance from RTLSR or RTLT model. (a,b) represent the red and NIR bands. (1) and (2) represent the RTLSR and RTLT models, respectively.

The optimized performance of the RTLSRS model compared to the RTLSR model over the snow and ice lands (IGBP = 15) is shown in Figure 7. The horizontal and vertical axes of the figure indicate the RMSE exhibited by the RTLSR and RTLSRS models, respectively. This means that the fitting residual of the RTLSRS model is smaller than that of the RTLSR model in the site when the point is to the lower right of the 1:1 line. Similarly, if the point is on the upper left of the 1:1 line, it means that the fitting residual of the RTLSRS model is larger. Additionally, the darker orange color represents the larger OR of the RTLSRS model, while the darker blue color represents the larger negative OR. In the red (Figure 7a) and NIR (Figure 7b) bands, we can observe that most of the points appear in the lower right of the 1:1 line, which means that the RTLSRS model outperforms the RTLSR model at most of the sites. Among all sites, the max OR of 93.6% and 93.8% for the RTLSRS model were achieved in the red and NIR bands, respectively. The mean RMSE of the RTLSR model can reach 0.0413 and 0.0450 in the red and NIR bands, while the mean RMSE of the RTLSRS model are only 0.0248 and 0.0261. These results suggest that the RTLSRS model

can better characterize the bidirectional reflectance of the snow and ice surface, which should effectively reduce the fitting residuals of the snow and ice covered sites.

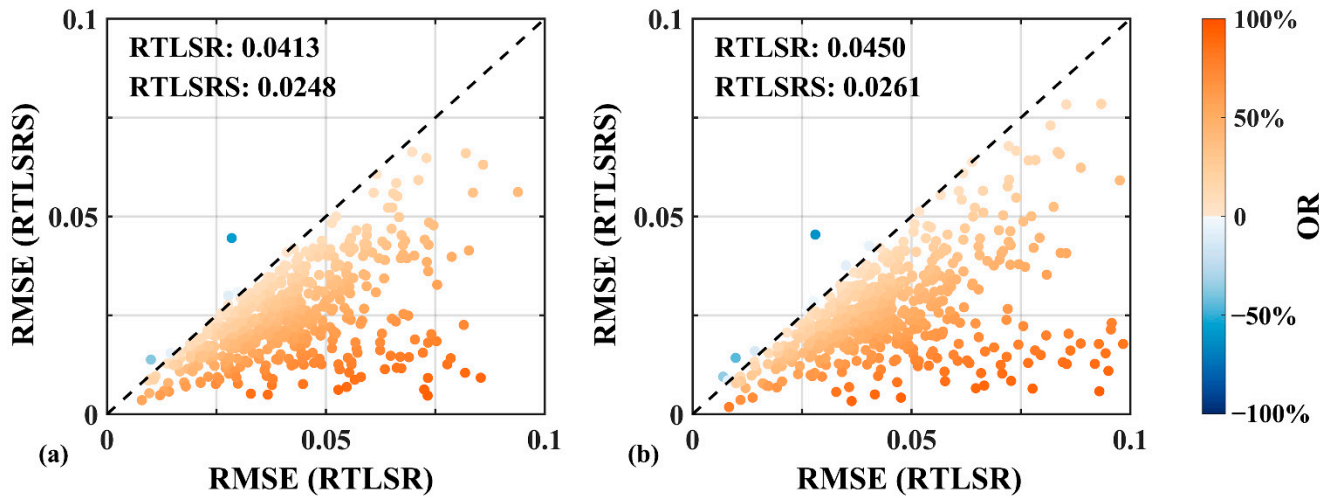


Figure 7. Comparison results of the RTLSR and RTLSRS models using data where IGBP is 15 in the POLDER database. Each point represents an observation site. The colors correspond to OR. The horizontal and vertical axes represent the RMSE of the RTLSR and RTLSRS models. The numbers marked in the upper-left corner are the mean RMSE of the RTLSR and the RTLSRS models. (a,b) represent the red and NIR bands, respectively.

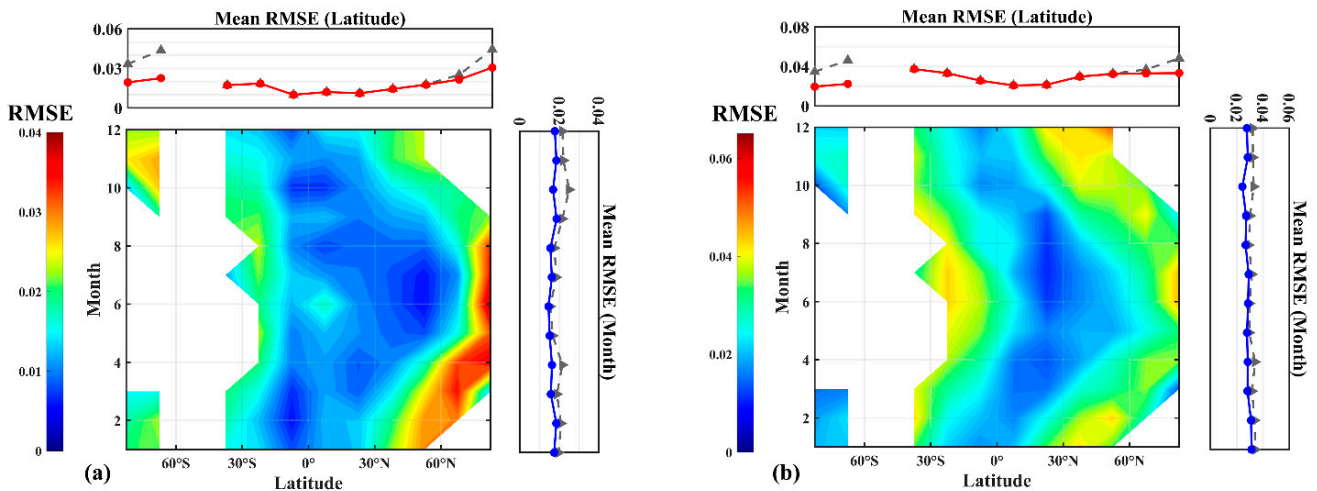


Figure 8. Comparison of the fitting residuals of the SJRS at different latitudes and months in the red (a) and NIR (b) bands. The colored bars represent RMSE values. The mean RMSE variation in different latitudes and months in the two bands are shown in the line plots above and to the right of the heatmaps, respectively. The gray lines in the line plots represent the mean RMSE of the RTLSR model, they are the same as the lines in Figure 5.

We compared the differences between using a single RTLSR model and the SJRS using the three kernel-driven models in Figure 8, which uses the same form as Figure 5 to show the fitting residuals for using the hybrid retrieval strategy at different latitudes and months. As can be seen in Figure 8, the fitting residuals of the SJRS are significantly reduced at high latitudes compared to using a single RTLSR model, in comparison to Figure 5. In the Antarctic region, for example, the mean RMSE of the RTLSR model reaches 0.0333 ($90^{\circ} S < \text{latitude} < 75^{\circ} S$) and 0.0438 ($75^{\circ} S < \text{latitude} < 60^{\circ} S$) in the red band, while the mean RMSE of SJRS is only 0.0194 and 0.0226, respectively. In the NIR band, the mean RMSE of the RTLSR model can reach 0.0347 ($90^{\circ} S < \text{latitude} < 75^{\circ} S$) and 0.0463

($75^\circ \text{ S} < \text{latitude} < 60^\circ \text{ S}$), while the mean RMSE of SJRS is only 0.0196 and 0.0225. Similarly, in the Arctic region, the SJRS is also effective in reducing the fitting residuals. Comparing the mean RMSE from different months, the mean RMSE of SJRS are smaller than those of the RTLSR model. These suggest that the SJRS using the three kernel-driven models can effectively compensate for the shortcomings of the retrieval method using a single RTLSR model.

4. Discussion

4.1. Applicability Differences of the RTLSR Strategy

In the results section, the RTLSR model shows a large applicability gap under different observation conditions. There are two important factors: (1) the type of land cover and vegetation cover density, and (2) the SZAs of reflectance used for the retrieval. These two factors cause the RTLSR model to exhibit larger fitting residuals at high latitudes (RMSE can reach up to 0.1 in some pixels, which is also a large fitting residual even for the snow surface). In this section, we discuss why the RTLSR model is significantly influenced by these two factors. Additionally, the impact of the applicability differences on the application of the RTLSR model is illustrated.

The kernel-driven model is a semi-empirical model with the kernels that provide physical condition constraints for an empirical fit. The approximate physical basis on which the kernels rest constrains, in a meaningful way, the possible BRDF shapes in unobserved regions of the viewing and illumination hemisphere. Therefore, the RossThick and LiSparseR kernels of the RTLSR model are the keys to its applicability in different conditions. The RossThick kernel was derived based on the radiative transfer theory of Ross [8], which is used to calculate the bidirectional reflectance above a horizontally homogeneous plant canopy [35]. Additionally, the LiSparseR kernel is the approximation of a geometric-optical model, which is used to describe the bidirectional properties of discrete canopies [9]. This means that the two kernels are both more suitable for vegetated lands and cannot capture large forward scattering, which is why the RTLSR model exhibits large fitting residuals on snow surfaces and urban and built-up lands. Additionally, it is clear why the fitting residuals of the RTLSR model are negatively correlated with vegetation cover density. The RTLSR model performs poorly over evergreen needleleaf forests due to the clumped (nonrandom) arrangement of the needle area in the crown [40], which is inconsistent with the assumptions in the RossThick kernel. For the second factor (the SZAs of reflectance used for retrieval), this may be due to the longer path of photons through the canopy caused by large SZA [41], and the extinction process becomes more complicated, resulting in more difficult modeling of the bidirectional reflectance [17]. Under the influence of the superposition of the two factors, the RTLSR model shows poorer applicability at high latitudes.

Currently, in most BRDF/Albedo global product productions and related large-scale researches, a single kernel-driven model was used. They did not take into account the difference in applicability of a single model under different conditions. This would lead to different absolute accuracies in different regions in the global product. Meanwhile, this may also lead to erroneous conclusions in large-scale researches. Taking the RTLSR model used in the experiments of this paper as an example, it exhibits a large difference in absolute accuracy on vegetated lands and snow surfaces. When it is applied to high altitude mountains, there may be a problem of a large gap of retrieval accuracy. This cannot be neglected in studies. Therefore, for this type of study, different models should be used in a targeted manner to ensure the best performance.

Many scholars developed many new kernels and kernel-driven models to improve the applicability of the models, which are summarized in Appendix A. These studies provide a rationale for the joint application of multiple models. In this paper, we tried to use the SJRS for a large-scale retrieval. The results show that this approach is effective in reducing the applicability differences. Therefore, we believe that this direction has great potential for exploration, which may be a better choice for global product production and large-scale researches.

4.2. Future Development and Application of the Kernel-Driven Models

Compared to the physical model, the semi-empirical kernel-driven models do not need to describe the details of the physical processes of light scattering in the scene and do not require too much prior knowledge of the scene parameters. At the same time, the linearly weighted form of the kernel-driven models allows for fast retrieval, making it easier to apply to large-scale experimental data processing than other models. This is the main reason why the kernel-driven models have been adopted by many sensors [9].

However, the existing kernels of the kernel-driven models are all based on a physical approximation of a particular hypothetical scenario. This means that the kernels have similar characteristics to the physical model: no kernel is equally suitable for every scenario. They have different adaptability for different scenarios. When the application scenario is closer to the assumed, the kernel-driven model is able to retrieve the results more accurately. On the contrary, if the application scenario deviates significantly from the kernel assumptions, the kernel-driven model exhibits poor adaptability. As demonstrated in the results section, the RTLSR model based on the vegetation cover scenario assumptions exhibit large fit residuals in the non-vegetation cover scenario. On the contrary, the RTLSRS model designed to describe the large forward scattering of the snow surface shows better fitting results at the sites with IGBP = 15 (snow and ice).

As mentioned in Appendix A for the numerous kernels and improved kernel-driven models, they are designed to be better adapted to a certain scenario. However, most of the existing BRDF/albedo products are produced by a single kernel-driven model, which inevitably leads to different degrees of fitting residuals under different observational conditions. Many studies that adopted kernel-driven models have also directly used the so-called widely used kernel-driven model without screening comparisons, which may also have the problem of adaptation differences. Therefore, there are several issues worth noting in future research work on kernel-driven models: (1) more comprehensive comparisons and evaluations of existing models are necessary to inform the selection of models for application; (2) in global product productions and large-scale studies, we should try to combine different models for different application scenarios, which can compensate for the shortcomings of the results due to the difference in adaptability; and (3) future work on the improvement of the kernel-driven models or their kernels may allow for more refined assumptions and modeling, which could improve the accuracy of retrieval. Although this would require more input parameters and prior knowledge, the development of existing computational power should be fully satisfying.

4.3. Limitations of the Study and Future Work

There are still some limitations in this study. First, the applicability comparison for the RTLSR model may be influenced by the coarser resolution of the POLDER-3 sensor ($6 \text{ km} \times 7 \text{ km}$). Therefore, the conclusions obtained may be unacceptable at other scales. Second, in this study, we focused only on the red and NIR bands. The ground substance has different spectral properties for different wavelengths. Therefore, the proposed joint-use strategy based on the results in the red and NIR bands may not be applicable for other bands. Third, while SJRS performs better at high latitudes, it is only a simple combination of three kernel-driven models, so more rigorous validations and optimizations are necessary for practical application in the future.

To address the limitations of this paper and some of the problems facing the field, our future work will focus on the following: (1) we will conduct a more comprehensive comparison and evaluation of the existing models and summarize a set of model selection references, and (2) use targeted modeling to address the shortcomings of existing models and attempt to propose a set of joint retrieval strategies applicable to various global observational conditions.

5. Conclusions

This study comprehensively compared the applicability of the kernel-driven model represented by the RTLSR kernels to revisit its performance under different observational conditions using the filtered high-quality POLDER BRDF database. Further, we explored the potential for the joint application of multiple kernel-driven models. The results show that the RTLSR model performs well which has small RMSE under most observational conditions. However, over different land covers, the RTLSR model has a better fitting ability over densely vegetated surfaces, while it shows more than twice as many fitting residuals on non-vegetated lands compared to vegetated. Under different sun-sensor geometries, the fitting residuals are positively correlated with SZA. The RTLSR model shows poorer fitting ability when SZA is large. Therefore, the RTLSR model shows better fitting ability at mid and low latitudes due to the better observational conditions. In contrast, the RTLSR model exhibits larger fitting residuals at high latitudes due to the increased proportion of non-vegetation covered lands and large SZA observational conditions. As an exploration, we proposed a model combination strategy, SJRS, by combining different models using the distinguishing indexes. The SJRS shows better performance at high latitudes. Based on this, we analyzed in depth the root causes for the differences in applicability of RTLSR models and the development potential of the joint application of multiple kernel-driven models. Additionally, we discussed the future direction of the kernel-driven models. These conclusions contribute to a better understanding of the fitting ability of the RTLSR model and are helping to improve the use of kernel-driven models. The proposed view of joint application of models also has the potential to improve the ability to describe the anisotropy of land surface reflectance.

Author Contributions: Conceptualization, K.Y. and S.G.; methodology, W.S.; software, H.L.; validation, X.M.; formal analysis, H.L.; investigation, X.M.; resources, K.Y.; writing—original draft preparation, H.L.; writing—review and editing, K.Y. and W.S.; visualization, H.L.; supervision, K.Y. and S.G.; project administration, K.Y. and X.M.; funding acquisition, K.Y. All authors have read and agreed to the published version of the manuscript.

Funding: This research was funded by the National Natural Science Foundation of China, grant number 41901298 and 42171305, and the Fundamental Research Funds for the Central Universities, grant number 265QZ2022001.

Institutional Review Board Statement: Not applicable.

Informed Consent Statement: Not applicable.

Data Availability Statement: Not applicable.

Conflicts of Interest: The authors declare no conflict of interest.

Abbreviations

List of abbreviations and their meanings in this paper.

Abbreviation	Meaning
Aero	Aerosol (a non-quantitative indication of the aerosol load in the used database)
ART	Asymptotic Radiative Transfer
AMBRALS	Algorithm for Model Bidirectional Reflectance Anisotropies of the Land Surface
BRDF	Bidirectional Reflectance Distribution Function; in this paper, it is used to represent the distribution of bidirectional reflectance
IGBP	International Geosphere-Biosphere Programme
KDST	Kernel-Driven model for Sloping Terrain
LAI	Leaf Area Index
MODIS	Moderate Resolution Imaging Spectroradiometer
NDVI	Normalized Difference Vegetation Index
NDVI _{per}	A threshold parameter; in this paper, it means the percentage of NDVI < 0 of the eligible observations at the site

Abbreviation	Meaning
NIR	Near-Infrared
OR	Optimization Ratio
PARASOL	Polarization and Anisotropy of Reflectances for Atmospheric Sciences coupled with Observations from a Lidar
POLDER	Polarization and Directionality of the Earth's Reflectances
RAA	Relative Azimuth Angle
RE	Relative Error
RMSE	Root-Mean-Square-Error
RTC	RossThickChen
RTLSR	RossThick-LiSparseReciprocal
RTLSRS	RossThick-LiSparseReciprocal-Snow
RTLTL	RossThick-LiTransit
RTM	RossThickMaignan
SJRS	Simple Joint Retrieval Strategy
SZA	Solar Zenith Angle
SZA _{mean}	A threshold parameter in this paper, it is the mean SZA of eligible observations at the site
TCKD	Topography-Coupled Kernel-Driven
TIR	Thermal Infrared
Topo-KD	Topographic Kernel-Driven
VZA	View Zenith Angle

Appendix A

The volume-scattering and geometric-optical kernels within the kernel-driven model are key to constraining the BRDF shape. Scholars have made a lot of contributions to improve the retrieval accuracy of the kernel-driven models to cope with different situations for more than two decades. In this subsection, we briefly reviewed the works on the improvement of the kernel-driven models and summarized it in two parts based on the improved methods: (1) the development of the new volume-scattering and geometric-optical kernels for the models, and (2) the extended forms of the kernel-driven model to fit certain conditions.

Appendix A.1. Development of Kernels

The existing volume-scattering kernels are developed based on the radiative transfer theory from Ross [35], including the original RossThick, RossThin kernels, and their improved forms from Maignan et al. and Jiao et al. [19,42]. The original RossThick and RossThin kernels were derived by Roujean et al. [8] and Wanner et al. [9], respectively. The two kernels are derived based on an approximation for the large (RossThick) and small (RossThin) values of the LAI to describe the radiative transfer processes in the dense and sparse canopy. Although the two kernels can model the radiative transfer processes within the canopy well, they do not take into account the hotspot effect, which makes the kernel-driven models usually underestimate the reflectance around the hotspot. To address this issue, Maignan et al. [43] and Jiao et al. [44] corrected the RossThick kernel as the RossThickMaignan (RTM) and RossThickChen (RTC) kernels, respectively. Maignan et al. [19] added a hotspot factor derived by Bréon et al. [43] based on the mutual shadowing theory by Jupp and Strahler [45] to generate the RTM kernel. Similarly, the RTC kernel developed by Jiao et al. [44] adds a hotspot factor in the RossThick kernel based on the theory of Chen and Cihlar. In the two kernels, ζ_0 , C_h , C_1 and C_2 are the parameters used to describe the shape of the hotspot. The RTM and RTC kernels have a better fitting ability around the hotspot direction compared to the original RossThick kernel.

The existing geometric-optical kernels include the Roujean kernel [8] and a series of Li kernels [6,9,17]. In the Roujean kernel derived by Roujean et al. [8], the reflectance is modeled for a random arrangement of rectangular protrusions on a flat horizontal surface. The LiSparse kernel models the reflectance of a sparse canopy scene by the areal proportions

of the sunlit crown, sunlit ground, shaded crown, and shaded ground. This kernel does not consider mutual shadowing, which cannot be disregarded in the dense canopy case. Therefore, the LiDense kernel is developed for the dense canopy. LiSparse, LiSparseR, and LiTransit kernels were introduced above [6,9].

The expressions for all kernels are given in Table A1.

Table A1. The common volume-scattering and geometric-optical kernels.

Types	Kernel Names	Kernel Expressions	Kernel Characteristics
K_{vol}	RossThick	$K_{RossThick} = \frac{(\frac{\pi}{2} - \xi) \cos \xi + \sin \xi}{\cos \theta_s + \cos \theta_v} - \frac{\pi}{4}$	Derived based on an approximation for the large value of the LAI to describe the radiative transfer processes in the dense canopy.
	RossThin	$K_{RossThin} = \frac{(\frac{\pi}{2} - \xi) \cos \xi + \sin \xi}{\cos \theta_s \cdot \cos \theta_v} - \frac{\pi}{2}$	Derived based on an approximation for the large value of the LAI to describe the radiative transfer processes in the sparse canopy.
	RossThickMaignan	$K_{RTM} = \frac{(\frac{\pi}{2} - \xi) \cos \xi + \sin \xi}{\cos \theta_s + \cos \theta_v} \times \left[1 + C_H \left(1 + \frac{\xi}{\xi_0} \right)^{-1} \right] - \frac{\pi}{4}$	Derived from the RossThick kernel by adding a hotspot factor based on the mutual shadowing theory. It can describe the hotspot effect compared to RossThick.
	RossThickChen	$K_{RTC} = \frac{(\frac{\pi}{2} - \xi) \cos \xi + \sin \xi}{\cos \theta_s + \cos \theta_v} \times \left[1 + C_1 e^{-\frac{\xi}{C_2}} \right] - \frac{\pi}{4}$	Derived from the RossThick kernel by adding a hotspot factor based on the theory of Chen and Cihlar [44]. It can describe the hotspot effect compared to RossThick.
K_{geo}	Roujean	$K_{Roujean} = \frac{1}{2\pi} \left[(\pi - \varphi) \cos \varphi + \sin \varphi \right] \frac{\tan \theta_s \tan \theta_v}{\tan^2 \theta_s + \tan^2 \theta_v - 2 \tan \theta_s \tan \theta_v \cos \varphi}$	The kernel is modeled for a random arrangement of rectangular protrusions on a flat horizontal surface.
	LiSparse	$K_{LiSparse} = O(\theta_s', \theta_v', \varphi) - \sec \theta_s' - \sec \theta_v' + \frac{1}{2} (1 + \cos \xi') \sec \theta_v'$	The kernel is modeled for a sparse canopy scene by the areal proportions of the sunlit crown, sunlit ground, shaded crown, and shaded ground.
	LiSparseR	$K_{LiSparseR} = O(\theta_s', \theta_v', \varphi) - \sec \theta_s' - \sec \theta_v' + \frac{1}{2} (1 + \cos \xi') \sec \theta_s' \sec \theta_v'$	The reciprocal form of the LiSparse kernel. It has a better extrapolation ability compared to LiSparse.
	LiDense	$K_{LiDense} = \frac{(1 + \cos \xi'') \sec \theta_v'}{\sec \theta_s' + \sec \theta_v' - O(\theta_s', \theta_v', \varphi)} - 2$	The kernel is similar as the LiSparse kernel, but for a dense canopy scene.
	LiDenseR	$K_{LiDenseR} = \frac{(1 + \cos \xi'') \sec \theta_s' \sec \theta_v'}{\sec \theta_s' + \sec \theta_v' - O(\theta_s', \theta_v', \varphi)} - 2$	The reciprocal form of the LiDense kernel. It has a better extrapolation ability compared to LiDense.
	LiTransit	$K_{LiTransit} = \begin{cases} K_{LiSparse}, & B(\theta_s', \theta_v', \varphi) \leq 2 \\ \frac{2 \cdot K_{LiSparse}}{B(\theta_s', \theta_v', \varphi)}, & B(\theta_s', \theta_v', \varphi) > 2 \end{cases}$	A kernel that combines the LiSparse and LiDense kernels. It solves the problem of the poor extrapolation ability of the LiSparse kernel compared to the LiSparseR kernel better.

Appendix A.2. Other Forms of Kernel-Driven Models

An accurate description of surface anisotropy is important for radiative transfer modeling and the retrieval of surface parameters [7,46–48]. Additionally, due to the advantages of the kernel-driven models, scholars gradually started to focus on extending the models to more application areas. Scholars developed other forms of the kernel-driven model that greatly enhance its application in, for example, snow surfaces, mountainous areas, thermal infrared (TIR):

1. The snow surface has completely different bidirectional reflection characteristics compared to vegetation, which makes the traditional kernel-driven model exhibit large fitting residuals on the snow surface. The RTLSRS model mentioned above, developed by Jiao et al. [21], can better describe the bidirectional reflectance properties of the pure snow surface and greatly reduce the fitting residuals exhibited by the RTLSR model on the snow surface. The publication of the model makes the application

of the kernel-driven models in snow-covered high altitudes and high latitude areas more mature.

2. The kernels of the original kernel-driven model are based on the assumption of a flat surface. However, compared to the flat terrain, the upwelling and downwelling radiance distribution and the shading relationship between vegetations are significantly affected over rugged terrain. This makes traditional kernel-driven models exhibit poorer fitting accuracy in mountainous areas. Therefore, scholars conducted in-depth studies on the application of the kernel-driven models in mountainous areas and proposed the improved forms. For example, Wu et al. [49] rederived the forms of the kernels on the slope and further improved the model, called the KDST (Kernel-Driven model for Sloping Terrain) model, which can consider the terrain. An improved topography-coupled kernel-driven model called the TCKD, was developed by Hao et al. [33]. The TCKD model also takes into account the effect of the diffuse skylight and corrects it. Yan et al. [22] developed a topographic kernel-driven (Topo-KD) algorithm, which can choose whether to invoke a modified kernel-driven model that can take into account terrain effects, depending on the ruggedness of the terrain. These models further take into account topographic effects to make the kernel-driven models more applicable to mountainous areas and are important for ecological and environmental monitoring.
3. Cao et al. [50] obtained good results by considering the directionality properties of TIR with the kernel-driven model, and they added a degree of freedom to the original model to correct the hotspot effect. Their research extends the application of kernel-driven models in the field of TIR.

In addition, researchers also used the models to correct the effect of large leaf inclination on canopy reflectance and the diffuse skylight on ground-based multi-angle measurements [51,52].

References

1. Nicodemus, F.E.; Richmond, J.C.; Hsia, J.J.; Ginsberg, I.W.; Limperis, T. Geometrical Considerations and Nomenclature for Reflectance. In *Final Report National Bureau of Standards*; US Department of Commerce, National Bureau of Standards: Washington, DC, USA, 1977; Volume 160.
2. Schaepman-Strub, G.; Schaepman, M.E.; Painter, T.H.; Dangel, S.; Martonchik, J.V. Reflectance quantities in optical remote sensing—definitions and case studies. *Remote Sens. Environ.* **2006**, *103*, 27–42. [[CrossRef](#)]
3. Tanioka, Y.; Cai, Y.; Ida, H.; Hirota, M. A spatial relationship between canopy and understory leaf area index in an old-growth cool-temperate deciduous forest. *Forests* **2020**, *11*, 1037. [[CrossRef](#)]
4. Xu, B.; Park, T.; Yan, K.; Chen, C.; Zeng, Y.; Song, W.; Yin, G.; Li, J.; Liu, Q.; Knyazikhin, Y. Analysis of global LAI/FPAR products from VIIRS and MODIS sensors for spatio-temporal consistency and uncertainty from 2012–2016. *Forests* **2018**, *9*, 73. [[CrossRef](#)]
5. Pokrovsky, O.; Roujean, J.-L. Land surface albedo retrieval via kernel-based BRDF modeling: I. Statistical inversion method and model comparison. *Remote Sens. Environ.* **2003**, *84*, 100–119. [[CrossRef](#)]
6. Lucht, W.; Schaaf, C.B.; Strahler, A.H. An algorithm for the retrieval of albedo from space using semiempirical BRDF models. *IEEE Trans. Geosci. Remote Sens.* **2000**, *38*, 977–998. [[CrossRef](#)]
7. Dickinson, R.E. Land processes in climate models. *Remote Sens. Environ.* **1995**, *51*, 27–38. [[CrossRef](#)]
8. Roujean, J.L.; Leroy, M.; Deschamps, P.Y. A bidirectional reflectance model of the Earth's surface for the correction of remote sensing data. *J. Geophys. Res. Atmos.* **1992**, *97*, 20455–20468. [[CrossRef](#)]
9. Wanner, W.; Li, X.; Strahler, A. On the derivation of kernels for kernel-driven models of bidirectional reflectance. *J. Geophys. Res. Atmos.* **1995**, *100*, 21077–21089. [[CrossRef](#)]
10. Wanner, W.; Strahler, A.; Hu, B.; Lewis, P.; Muller, J.P.; Li, X.; Schaaf, C.B.; Barnsley, M. Global retrieval of bidirectional reflectance and albedo over land from EOS MODIS and MISR data: Theory and algorithm. *J. Geophys. Res. Atmos.* **1997**, *102*, 17143–17161. [[CrossRef](#)]
11. Schaaf, C.B.; Gao, F.; Strahler, A.H.; Lucht, W.; Li, X.; Tsang, T.; Strugnell, N.C.; Zhang, X.; Jin, Y.; Muller, J.-P. First operational BRDF, albedo nadir reflectance products from MODIS. *Remote Sens. Environ.* **2002**, *83*, 135–148. [[CrossRef](#)]
12. Schaaf, C.; Liu, J.; Gao, F.; Strahler, A.H. MODIS albedo and reflectance anisotropy products from Aqua and Terra. *Land Remote Sens. Glob. Environ. Chang. NASA's Earth Obs. Syst. Sci. ASTER MODIS* **2011**, *11*, 549–561.
13. Wang, Z.; Schaaf, C.B.; Sun, Q.; Shuai, Y.; Román, M.O. Capturing rapid land surface dynamics with Collection V006 MODIS BRDF/NBAR/Albedo (MCD43) products. *Remote Sens. Environ.* **2018**, *207*, 50–64. [[CrossRef](#)]

14. Deschamps, P.-Y.; Bréon, F.-M.; Leroy, M.; Podaire, A.; Bricaud, A.; Buriez, J.-C.; Seze, G. The POLDER mission: Instrument characteristics and scientific objectives. *IEEE Trans. Geosci. Remote Sens.* **1994**, *32*, 598–615. [[CrossRef](#)]
15. Bicheron, P.; Leroy, M. Bidirectional reflectance distribution function signatures of major biomes observed from space. *J. Geophys. Res. Atmos.* **2000**, *105*, 26669–26681. [[CrossRef](#)]
16. Bacour, C.; Bréon, F.-M. Variability of biome reflectance directional signatures as seen by POLDER. *Remote Sens. Environ.* **2005**, *98*, 80–95. [[CrossRef](#)]
17. Li, X.; Gao, F.; Chen, L.; Strahler, A.H. Derivation and validation of a new kernel for kernel-driven BRDF models. In *Remote Sensing for Earth Science, Ocean, and Sea Ice Applications*; International Society for Optics and Photonics: Bellingham, DC, USA, 1999; pp. 368–379.
18. Gao, F.; Li, X.; Strahler, A.; Schaaf, C. Evaluation of the Li transit kernel for BRDF modeling. *Remote Sens. Rev.* **2000**, *19*, 205–224. [[CrossRef](#)]
19. Maignan, F.; Bréon, F.-M.; Lacaze, R. Bidirectional reflectance of Earth targets: Evaluation of analytical models using a large set of spaceborne measurements with emphasis on the Hot Spot. *Remote Sens. Environ.* **2004**, *90*, 210–220. [[CrossRef](#)]
20. Jiao, Z.; Dong, Y.; Li, X. An approach to improve hot spot effect for the MODIS BRDF/Albedo algorithm. In *Proceedings of the 2013 IEEE International Geoscience and Remote Sensing Symposium-IGARSS, Melbourne, Australia, 21–26 July 2013*; pp. 3037–3039.
21. Jiao, Z.; Ding, A.; Kokhanovsky, A.; Schaaf, C.; Bréon, F.-M.; Dong, Y.; Wang, Z.; Liu, Y.; Zhang, X.; Yin, S.; et al. Development of a snow kernel to better model the anisotropic reflectance of pure snow in a kernel-driven BRDF model framework. *Remote Sens. Environ.* **2019**, *221*, 198–209. [[CrossRef](#)]
22. Yan, K.; Li, H.; Song, W.; Tong, Y.; Hao, D.; Zeng, Y.; Mu, X.; Yan, G.; Fang, Y.; Myneni, R.B. Extending a Linear Kernel-Driven BRDF Model to Realistically Simulate Reflectance Anisotropy Over Rugged Terrain. *IEEE Trans. Geosci. Remote Sens.* **2021**, *60*, 1–16. [[CrossRef](#)]
23. Hu, B.; Wanner, W.; Li, X.; Strahler, A.H. Validation of kernel-driven semiempirical BRDF models for application to MODIS/MISR data. In *Proceedings of the IGARSS'96, 1996 International Geoscience and Remote Sensing Symposium, Lincoln, NE, USA, 27–31 May 1996*; pp. 1669–1671.
24. Hu, B.; Lucht, W.; Li, X.; Strahler, A.H. Validation of kernel-driven semiempirical models for the surface bidirectional reflectance distribution function of land surfaces. *Remote Sens. Environ.* **1997**, *62*, 201–214. [[CrossRef](#)]
25. Huang, X.; Jiao, Z.; Dong, Y.; Zhang, H.; Li, X. Analysis of BRDF and Albedo Retrieved by Kernel-Driven Models Using Field Measurements. *IEEE J. Sel. Top. Appl. Earth Obs. Remote Sens.* **2013**, *6*, 149–161. [[CrossRef](#)]
26. Breon, F.-M.; Maignan, F. A BRDF-BPDF database for the analysis of Earth target reflectances. *Earth Syst. Sci. Data* **2017**, *9*, 31–45. [[CrossRef](#)]
27. Liu, S.; Yan, L.; Yang, B. Degree of Linear Polarization of Land Surfaces: Analyses Using POLDER/PARASOL Measurements. *IEEE Access* **2020**, *8*, 200561–200572. [[CrossRef](#)]
28. Ye, L.; Xiao, P.; Zhang, X.; Feng, X.; Hu, R.; Ma, W.; Li, H.; Song, Y.; Ma, T. Evaluating Snow Bidirectional Reflectance of Models Using Multiangle Remote Sensing Data and Field Measurements. *IEEE Geosci. Remote Sens. Lett.* **2020**, *19*, 1–5. [[CrossRef](#)]
29. Chopping, M.; Moisen, G.G.; Su, L.; Laliberte, A.; Rango, A.; Martonchik, J.V.; Peters, D.P.C. Large area mapping of southwestern forest crown cover, canopy height, and biomass using the NASA Multiangle Imaging Spectro-Radiometer. *Remote Sens. Environ.* **2008**, *112*, 2051–2063. [[CrossRef](#)]
30. Hilker, T.; Coops, N.C.; Hall, F.G.; Black, T.A.; Wulder, M.A.; Nesic, Z.; Krishnan, P. Separating physiologically and directionally induced changes in PRI using BRDF models. *Remote Sens. Environ.* **2008**, *112*, 2777–2788. [[CrossRef](#)]
31. Liang, S.; Li, X.; Wang, J. *Quantitative Remote Sensing: Concepts and Algorithms*; Science Press: Beijing, China, 2013.
32. Wu, S.; Wen, J.; Gastellu-Etchegorry, J.-P.; Liu, Q.; You, D.; Xiao, Q.; Hao, D.; Lin, X.; Yin, T. The definition of remotely sensed reflectance quantities suitable for rugged terrain. *Remote Sens. Environ.* **2019**, *225*, 403–415. [[CrossRef](#)]
33. Hao, D.; Wen, J.; Xiao, Q.; You, D.; Tang, Y. An Improved Topography-Coupled Kernel-Driven Model for Land Surface Anisotropic Reflectance. *IEEE Trans. Geosci. Remote Sens.* **2020**, *58*, 2833–2847. [[CrossRef](#)]
34. Lucht, W.; Roujean, J.L. Considerations in the parametric modeling of BRDF and albedo from multiangular satellite sensor observations. *Remote Sens. Rev.* **2000**, *18*, 343–379. [[CrossRef](#)]
35. Ross, J. *The Radiation Regime and Architecture of Plant Stands*; Springer Science & Business Media: Berlin/Heidelberg, Germany, 1981.
36. Lucht, W. Expected retrieval accuracies of bidirectional reflectance and albedo from EOS-MODIS and MISR angular sampling. *J. Geophys. Res. Atmos.* **1998**, *103*, 8763–8778. [[CrossRef](#)]
37. Li, X.; Strahler, A.H. Geometric-optical bidirectional reflectance modeling of the discrete crown vegetation canopy: Effect of crown shape and mutual shadowing. *IEEE Trans. Geosci. Remote Sens.* **1992**, *30*, 276–292. [[CrossRef](#)]
38. Lucht, W. *AMBRALS User's Guide. Version 3.0*; Center for Remote Sensing: Boston, MA, USA, 1998.
39. Li, X.; Wang, J.; Strahler, A.H. Apparent reciprocity failure in directional reflectance of structured surfaces. *Prog. Nat. Sci. Beijing* **1999**, *9*, 747–752.
40. Stenberg, P. Correcting LAI-2000 estimates for the clumping of needles in shoots of conifers. *Agric. For. Meteorol.* **1996**, *79*, 1–8. [[CrossRef](#)]
41. Yin, G.; Li, A.; Zhao, W.; Jin, H.; Bian, J.; Wu, S. Modeling canopy reflectance over sloping terrain based on path length correction. *IEEE Trans. Geosci. Remote Sens.* **2017**, *55*, 4597–4609. [[CrossRef](#)]

42. Jiao, Z.; Schaaf, C.B.; Dong, Y.; Román, M.; Hill, M.J.; Chen, J.M.; Wang, Z.; Zhang, H.; Saenz, E.; Poudyal, R.; et al. A method for improving hotspot directional signatures in BRDF models used for MODIS. *Remote Sens. Environ.* **2016**, *186*, 135–151. [[CrossRef](#)]
43. Bréon, F.M.; Maignan, F.; Leroy, M.; Grant, I. Analysis of hot spot directional signatures measured from space. *J. Geophys. Res. Atmos.* **2002**, *107*, AAC 1-1–AAC 1-15. [[CrossRef](#)]
44. Chen, J.; Cihlar, J. A hotspot function in a simple bidirectional reflectance model for satellite applications. *J. Geophys. Res. Atmos.* **1997**, *102*, 25907–25913. [[CrossRef](#)]
45. Jupp, D.L.; Strahler, A.H. A hotspot model for leaf canopies. *Remote Sens. Environ.* **1991**, *38*, 193–210. [[CrossRef](#)]
46. Wen, J.; Liu, Q.; Xiao, Q.; Liu, Q.; You, D.; Hao, D.; Wu, S.; Lin, X. Characterizing Land Surface Anisotropic Reflectance over Rugged Terrain: A Review of Concepts and Recent Developments. *Remote Sens.* **2018**, *10*, 370. [[CrossRef](#)]
47. Yan, K.; Pu, J.; Park, T.; Xu, B.; Zeng, Y.; Yan, G.; Weiss, M.; Knyazikhin, Y.; Myneni, R.B. Performance stability of the MODIS and VIIRS LAI algorithms inferred from analysis of long time series of products. *Remote Sens. Environ.* **2021**, *260*, 112438. [[CrossRef](#)]
48. Yan, K.; Zhang, Y.; Tong, Y.; Zeng, Y.; Pu, J.; Gao, S.; Li, L.; Mu, X.; Yan, G.; Rautiainen, M. Modeling the radiation regime of a discontinuous canopy based on the stochastic radiative transport theory: Modification, evaluation and validation. *Remote Sens. Environ.* **2021**, *267*, 112728. [[CrossRef](#)]
49. Wu, S.; Wen, J.; Xiao, Q.; Liu, Q.; Hao, D.; Lin, X.; You, D. Derivation of Kernel functions for Kernel-driven reflectance model over sloping terrain. *IEEE J. Sel. Top. Appl. Earth Obs. Remote Sens.* **2018**, *12*, 396–409. [[CrossRef](#)]
50. Cao, B.; Roujean, J.-L.; Gastellu-Etchegorry, J.-P.; Liu, Q.; Du, Y.; Lagouarde, J.-P.; Huang, H.; Li, H.; Bian, Z.; Hu, T. A general framework of kernel-driven modeling in the thermal infrared domain. *Remote Sens. Environ.* **2021**, *252*, 112157. [[CrossRef](#)]
51. Wu, S.; Wen, J.; Liu, Q.; You, D.; Yin, G.; Lin, X. Improving Kernel-Driven BRDF Model for Capturing Vegetation Canopy Reflectance with Large Leaf Inclinations. *IEEE J. Sel. Top. Appl. Earth Obs. Remote Sens.* **2020**, *13*, 2639–2655. [[CrossRef](#)]
52. Dong, Y.; Jiao, Z.; Ding, A.; Zhang, H.; Zhang, X.; Li, Y.; He, D.; Yin, S.; Cui, L. A modified version of the kernel-driven model for correcting the diffuse light of ground multi-angular measurements. *Remote Sens. Environ.* **2018**, *210*, 325–344. [[CrossRef](#)]